PERGAMON

Engineering Fracture Mechanics 67 (2000) 193–207

Engineering Fracture Mechanics

www.elsevier.com/locate/engfracmech

Influence of foreign-object damage on crack initiation and early crack growth during high-cycle fatigue of Ti–6Al–4V

J.O. Peters, R.O. Ritchie *

Department of Materials Science and Mineral Engineering, University of California, 463 Evans Hall 1760, Berkeley, CA 94720-1760, USA

Received 10 January 2000; received in revised form 4 May 2000; accepted 11 May 2000

Abstract

The objective of this work is to provide a rationale approach to define the limiting conditions for high-cycle fatigue (HCF) in the presence of foreign-object damage (FOD). This study focused on the role of simulated FOD in affecting the initiation and early growth of small surface fatigue cracks in a Ti–6Al–4V alloy, processed for typical turbine blade applications. Using high-velocity (200–300 m/s) impacts of 3.2 mm diameter steel spheres on the flat surface of fatigue test specimens to simulate FOD, it is found that the resistance to HCF is markedly reduced due to earlier crack initiation. Premature crack initiation and subsequent near-threshold crack growth is primarily affected by the stress concentration associated with the FOD indentation and the presence of small microcracks in the damaged zone (seen only at the higher impact velocities). Furthermore, the effect of residual stresses and microstructural damage from FOD-induced plastic deformation at the indent sites are assessed in terms of fatigue strength degradation. It is shown that FOD-initiated cracks, that are of a size comparable with microstructural dimensions, can propagate at applied stress-intensity ranges on the order of $\Delta K \sim 1$ MPa$\sqrt{\text{m}}$, i.e., a factor of roughly two less than the "worst-case" threshold stress-intensity range in Ti–6Al–4V for a crack of a size large compared to microstructural dimensions (a "continuum-sized" crack). Correspondingly, for FOD-initiated failures, where the critical condition for HCF must be defined in the presence of microstructurally small cracks, the Kitagawa–Takahashi diagram, with the limiting conditions of the stress-concentration corrected 10^7-cycle fatigue limit and the "worst-case" ΔK_{TH} fatigue threshold, is proposed as a basis for design against FOD-induced HCF failures.

Keywords: Foreign-object damage; High-cycle fatigue; Fatigue-crack growth threshold; Small cracks; Ti–6Al–4V

1. Introduction

The high-cycle fatigue (HCF) of aircraft gas-turbine engine components has traditionally been analyzed using a modified Goodman diagram approach; however, because of an increasing incidence of late of HCF-related engine failures, particularly involving titanium alloy fan and compressor blades, this approach is currently being re-evaluated [1–3]. Three major concerns have been identified, namely (i) interactions of low-cycle fatigue (LCF) and HCF loading, (ii) foreign-object damage (FOD) and (iii) fretting. All these

* Corresponding author. Tel.: +1-510-486-5798; fax: +1-510-486-4995.
E-mail address: roritchie@lbl.gov (R.O. Ritchie).

0013-7944/00/$ - see front matter
PII: S0013-7944(00)00045-X

factors can lead to premature fatigue crack initiation and growth, which can result in seemingly unpredictable *in service* failures, due to the high-frequency vibratory loading (>1 kHz) involved [3]. Consequently, design against HCF based on the damage-tolerant concept of a fatigue-crack growth threshold (ΔK_{TH}) for no crack growth would appear to offer a preferred approach; however, such thresholds must reflect representative HCF conditions of high frequencies, small crack sizes and, depending on the blade span location, very high mean stress levels [1–5].

FOD, from bird strikes or hard body impacts, e.g., stones, primarily on the fan blades, can cause (depending on the impact severity) immediate blade fracture [6] or damage from stress-raising notches [6–8], cracks [8] and deformation of the microstructure. In a recent study on Ti–6Al–4V [9] where FOD was simulated by the high-velocity impact of steel shot on a flat surface, such damage was found to markedly reduce the fatigue strength principally by causing the earlier initiation of fatigue cracks. Limiting conditions for potential HCF-related turbine blade failures were proposed based on the concept of a "worst-case" threshold for no fatigue-crack growth that applies strictly for "continuum-sized" cracks, i.e., large or physically small cracks with dimensions larger than the characteristic microstructural size-scales. The mechanistic effect of FOD on the fatigue-crack growth thresholds was assessed in terms of (i) stress concentration associated with the FOD indentation, (ii) FOD-induced small cracks in the damage zone, (iii) localized presence of impact damage associated residual stresses at locations of the preferred sites for crack initiation, and (iv) microstructural damage from FOD-induced plastic deformation. Of particular note was the observation of the formation of small microcracks in the damaged region of the higher velocity impacts; such microcracks provided preferred sites for premature crack initiation on subsequent fatiguing. However, the quantitative effect of these FOD-induced microcracks on the fatigue-crack growth threshold was not investigated.

The objective of the current study is specifically to examine the role of FOD-induced microcracks (~2–25 μm in surface length) on the earliest stages of FOD-induced fatigue failures in the same Ti–6Al–4V alloy, $\alpha + \beta$ processed for typical turbine blade applications. This is achieved by defining the limiting conditions for crack initiation and early fatigue-crack growth in the presence of such microcracks, in comparison to the fatigue threshold behavior of naturally initiated small ($2c \sim 45$–1000 μm) and large through-thickness (>5 mm) cracks in undamaged material.

2. Experimental procedures

2.1. Material

The titanium alloy Ti–6Al–4V under study, of chemical composition given in Table 1, was part of a set of forgings produced specifically for the US Air Force sponsored programs on HCF; its β-transus temperature is ~996°C. Mill annealed 63.5 mm diameter bar stock material was $\alpha + \beta$ forged in one stroke at 938°C on a closed-end channel die to a plate size of $400 \times 150 \times 20$ mm^3, followed by air-cooling. Subsequently, the forging plates were solution treated in an air furnace at 927°C for 1 h followed by fan-air cooling; this resulted in a cooling rate of ~200°C/min. Finally, the plates were stress relieved in vacuo for 2 h at 705°C. Additional material and processing details are given in Ref. [10]. The resulting bimodal microstructure of the plate material, consisting of a volume fraction of ~60% primary α (diameter ~20 μm) within a lamellar $\alpha + \beta$ matrix, is shown in Fig. 1; this condition has also been termed "solution treated and overaged" (STOA).

Table 1
Chemical composition of Ti–6Al–4V bar stock material in wt.% [10]

Ti	Al	V	Fe	O	N	H
Bal.	6.30	4.19	0.19	0.19	0.013	0.0041

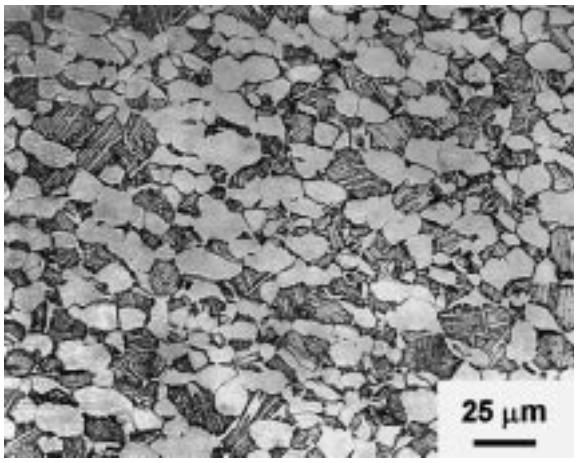

Fig. 1. Optical micrograph of the bimodal (STOA) microstructure of forged Ti–6Al–4V plate material (etched in 3.5% HNO_3–5% HF).

Table 2
Uniaxial tensile properties of bimodal Ti–6Al–4V[a]

E (GPa)	$\sigma_{0.2}$ (MPa)	UTS (MPa)	σ_F (MPa)	Tens. el. (%)	RA (%)
110	915	965	1310	19	45

[a] E: Young's modulus, $\sigma_{0.2}$: yield stress, UTS: ultimate tensile strength, σ_F: true fracture stress, Tens. el.: tensile elongation, RA: reduction of area at fracture; strain rate 8×10^{-4} s^{-1}.

To investigate microstructural changes caused by FOD impacts, transmission electron microscopy (TEM) foils were prepared by mechanical grinding in water and then thinned in a Fischione ion mill at 5 kV. For the impacted condition, the TEM foil location was parallel to the base of the indent (depth below indent is approximately 150 μm).

Uniaxial tensile properties, based on testing performed in the L-direction (parallel to the length of the plate) at an initial strain rate of 8×10^{-4} s^{-1}, are listed in Table 2.

2.2. Simulation of foreign-object damage

Foreign-object damage was simulated by firing 3.2 mm diameter chrome-hardened steel spheres onto a flat specimen surface of tensile fatigue (so-called modified K_B) specimens at an angle of 90° (normal impact, Fig. 2) at velocities of 200, 250 and 300 m/s using a compressed-gas gun facility. Impact velocities of 200–300 m/s represent typical *in-service* impact velocities on aircraft engine fan blades. Simulated impact crater dimensions by ballistic shots with 3.2 mm diameter steel spheres were found to generate damage, typical of *in-service* induced FOD notches; indeed, the resulting root radii were seen to correspond closely to surveyed *in-service* FOD root radii. [8] Further details of the 1.2 m-long compressed-gas gun test setup are given in Ref. [9].

2.3. Fatigue test methods

For an evaluation of the smooth-bar HCF limit of the bimodal Ti–6Al–4V alloy, in this study 1000 Hz stress-life (S–N) tests were performed on hourglass specimens (diameter: 5.4 mm). To minimize surface residual stresses and high dislocation density from specimen processing, specimens were chemically milled in a solution of 50 ml HF, 500 ml HNO_3 and 1500 ml H_2O for 30 min at ambient temperature. Specimen axis was parallel oriented to the length of the plate (L-direction).

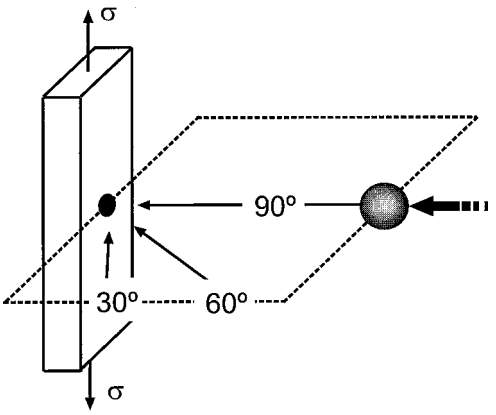

Fig. 2. Schematic illustration showing impact angles with respect to specimen geometry and loading axis for fatigue tests. In this study, a normal (90°) impact angle was chosen.

The effect of FOD on the fatigue behavior of Ti–6Al–4V was examined using modified K_B specimens. This sample has a rectangular cross-section of 3.2×7.2 mm^2, a gauge length of 20 mm and cylindrical buttonhead grips; it was originally developed by GE aircraft engines to assess fatigue performance in blade loading configurations [11]. A nominally stress-free surface in the gauge section was prepared using standard stress relief and chemical-milling procedures. As noted above, steel spheres were fired at high velocity at 90° to this surface to simulate FOD. After impact, specimens were subsequently cycled at 20 Hz (sinusoidal waveform) at a load ratio of $R = 0.1$ with a nominally maximum stress of 500 MPa. Preliminary tests were performed at nominal maximum stress values of 400 and 350 MPa at 20 Hz and 325 MPa at 1000 Hz. Throughout fatigue testing, specimens were periodically removed from the test frame and the progress of crack initiation and growth examined in a high-resolution LEO 1550 field-emission scanning electron microscope (SEM). To detect the initially small-sized FOD- and fatigue-induced surface cracks, the SEM was operated at a low beam voltage of 3 kV. For the present alloy, fractographic observations [9] revealed an approximate crack depth (a) to surface crack length ($2c$) ratio:

$$a/2c \sim 0.45 \quad (2c = 20\text{–}1000\ \mu\text{m}). \tag{1}$$

After converting the surface crack length ($2c$) into crack depth (a) according to Eq. (1), the rate of crack extension caused by the fatigue loading was computed using standard finite difference procedures (with no smoothing routines) and is expressed in terms of average crack extension per cycle ($\mathrm{d}a/\mathrm{d}N$).

Approximate local stress intensities for small cracks at base and crater rim of the indentation were calculated from the relationship of Lukáš [12] for small cracks at notches, which includes both indentation geometry and stress concentration effects:

$$\Delta K = \frac{0.7k_t}{\sqrt{1 + 4.5(a/\rho)}}\Delta\sigma\sqrt{\pi a}, \tag{2}$$

where k_t is the elastic stress-concentration factor, $\Delta\sigma$ is the stress range, a is the crack depth, and ρ is the indentation radius. The factor of 0.7 is based on the stress-intensity boundary correction and the crack-shape correction factors [12].

Elastic stress-concentration factors, k_t, surrounding the impact damage sites were determined based on three-dimensional photoelastic experiments performed by Nisida et al. [13]. It is assumed that the pile-up of material at crater rim has no effect on k_t, because of the relatively small height of the pile-up at the crater rim. The impact crater was treated like hemispherical hollow, with a depth corresponding to the distance

Table 3
Summary of test conditions[a]

Test no.	Impact velocity (m/s)	$\varnothing W$ (mm)	δ (mm)	Microcrack initiation	k_t base	k_t rim	σ_{max} (MPa)	$\Delta\sigma$ (MPa)	N_F (cycles)	k_f
1	300	2.67	0.67	Rim	1.60	1.25	500	450	3.4×10^4	1.65
2	300	2.67	0.67	Rim	1.60	1.25	500	450	4.6×10^4	1.55
3	300	2.67	0.67	Base[b]/rim	1.60	1.25	500	450	6.5×10^4	1.45
4	300	2.67	0.67	Rim	1.60	1.25	400	360	[c]	
5	300	2.67	0.67	Rim	1.60	1.25	350	315	[c]	
6	300	2.67	0.67	Rim	1.60	1.25	325	292.5	1.0×10^6	1.70
7	250	2.38	0.54	Base	1.50	1.20	500	450	8.0×10^4	1.40
8	250	2.38	0.54	Base	1.50	1.20	500	450	7.8×10^4	1.40
9	250	2.38	0.54	Base	1.50	1.20	500	450	8.2×10^4	1.40
10	200	2.14	0.43	Base	1.40	1.15	500	450	7.5×10^4	1.40
11	200	2.14	0.43	Base	1.40	1.15	500	450	1.4×10^5	1.30

[a] $\varnothing W$: chord width of impact crater, δ: indentation depth (measured from pile-up at the crater rim to the base of indentation), location of microcrack initiation, k_t: elastic stress-concentration factor, σ_{max}: maximum stress, $\Delta\sigma$: stress range, N_F: number of cycles at failure, k_f: effective-fatigue stress-concentration factor.
[b] Crack initiation at FOD-test-related Si particle at indent base.
[c] Load shedding test.

from the pile-up at the crater rim to the base of the indentation. Indeed, recently performed three-dimensional numerical analysis [14] gave identical k_t-values at the crater rim, but predicted values ~10% higher at the base of the indentations. Table 3 lists the impact site geometry dimensions and the resulting elastic stress-concentration factors according to photoelastic experiments [13], which reach a maximum value at the base of the indentation sites, i.e., ranging from $k_t = 1.6$ (for a 300 m/s impact site) to $k_t = 1.4$ (for a 200 m/s site). Corresponding values at the pile-up at the crater rim range from $k_t = 1.25$ (300 m/s) to $k_t = 1.15$ (200 m/s). Effective stress concentration factors, k_f, for FOD were estimated from the ratio of the maximum stress (at $R = 0.1$) in an undamaged, smooth-bar sample to the corresponding far-field maximum stress of a sample following simulated FOD damage to give the same life.

It should be noted that contributions to the stress-intensity values (Eq. (2)) from the residual stress field surrounding the indentation have not been taken into account, due to uncertainty in the value of these local residual stresses. Numerical analysis by Chen and Hutchinson [14] and experimental synchronous X-ray micro-diffraction studies at Berkeley [15] are currently focusing on this issue.

3. Results and discussion

3.1. Simulation of foreign-object damage

Typical damage sites caused by ballistic impacts of 3.2-mm steel spheres on flat surfaces under normal impact (90°) at impact velocities of 200 and 300 m/s are shown, respectively, in the scanning electron micrographs in Fig. 3a and b. The nature of the damage, as characterized by size and shape of the indents and location of microcracking, is a marked function of impact velocity, as listed in Table 3. At velocities above 250 m/s, a pronounced pile-up of material, some of it detached, is evident at the crater rim; in addition, circumferentially oriented intense shear bands are seen, emanating from the surface of the impact crater (Fig. 3b); such effects are not apparent for 200 m/s impacts (Fig. 3a). Moreover, for the high velocity impact at 300 m/s, plastic flow of material at the crater rim results in multiple micro-notches (Fig. 4a) and

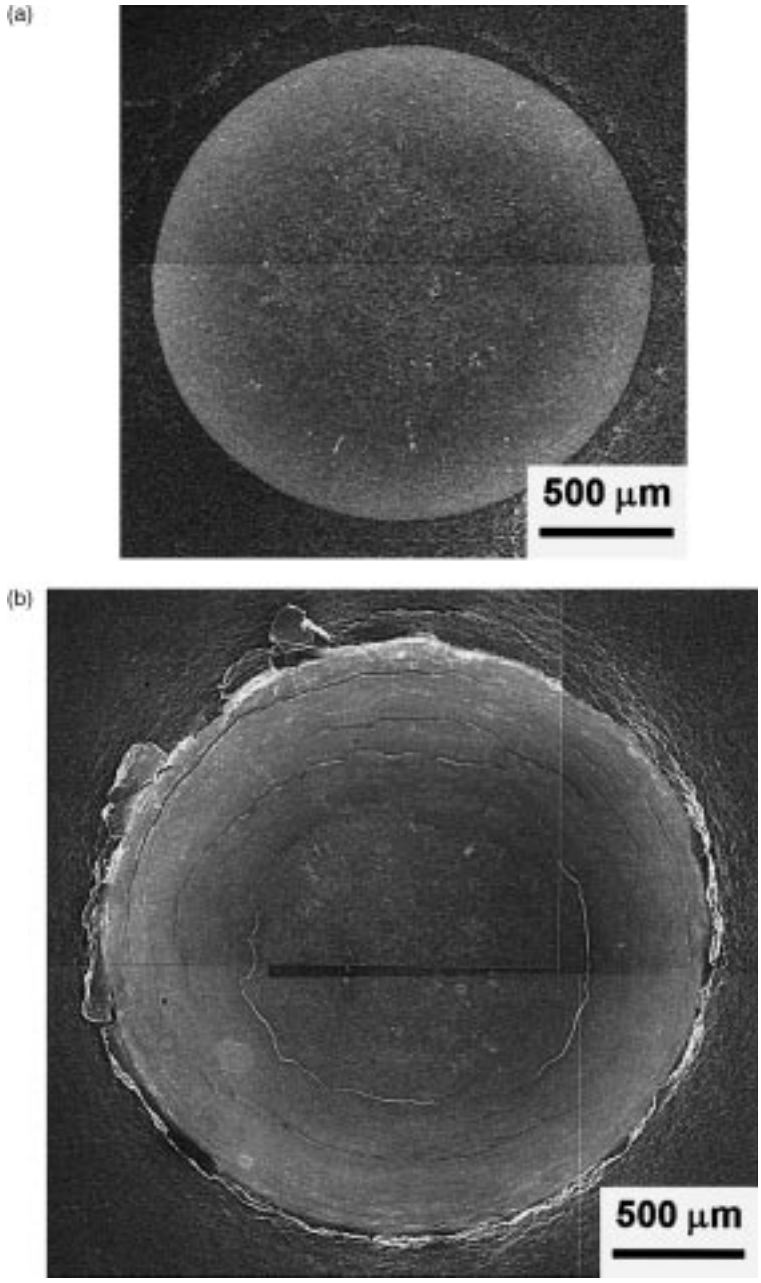

Fig. 3. Scanning electron micrographs of impact damage sites for (a) 200 m/s and (b) 300 m/s impact velocities, indicating increasing damage with increasing velocity with respect to indentation size, pile-up formation at crater rim and intense shear band formation emanating at the indent surface.

microcracking (Fig. 4b). The microcracks are quite small, i.e., between ~2 and 25 μm in surface length, but when favorably oriented with respect to the subsequently applied fatigue stress axis, they clearly provided the nucleation sites for high-cycle fatigue-crack growth (Fig. 4c). Such microcracking could not be detected

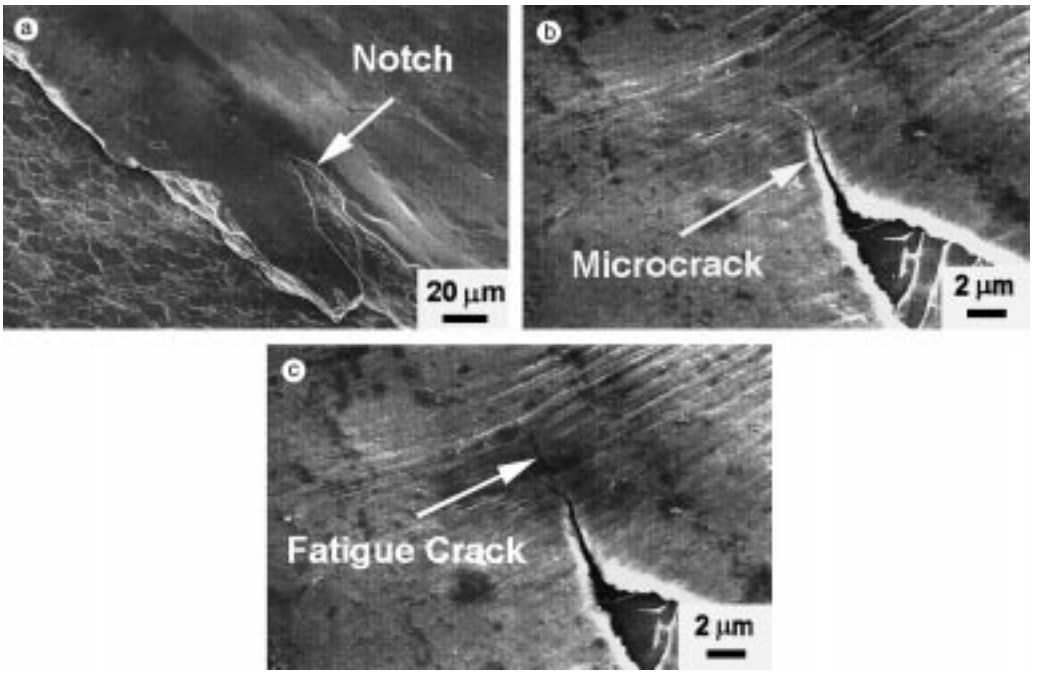

Fig. 4. Scanning electron micrographs showing the presence of microcracking at crater rim of an FOD indent after the highest velocity (300 m/s) impacts. Micrographs show (a) local notches at crater rim caused by plastic flow of material, (b) microcracks emanating from such notches, and (c) subsequent fatigue-crack growth initiated at such microcracks after $N = 5000$ cycles at nominal $\sigma_{max} = 500$ MPa ($R = 0.1$).

in this alloy at impact velocities below 250 m/s. This strongly implies that low velocity or quasi-static indentations do not provide a realistic simulation of FOD, because such lower velocity impacts do not necessarily induce all the damage processes associated with this phenomenon; specifically, FOD-induced microcracking is not seen in this alloy at impact velocities below ~250 m/s.

TEM was performed to investigate any microstructural changes caused by FOD impact. The undamaged microstructure (Fig. 5a) revealed in both the globular primary α phase and the $\alpha + \beta$ lamellar matrix (alternating α lamellae and β lamellae) a low dislocation density. The damaged microstructure following a ballistic impact is shown in Fig. 5b (TEM foil prepared from just below base of indentation). Both the primary α phase and the $\alpha + \beta$ lamellar matrix exhibit a very high dislocation density. It is evident that the impact loading introduces a very high density of dislocations below the indentation site, with some of the dislocations, specifically within the primary α phase, arranged in slip bands (see arrows, Fig. 5b).

3.2. Fatigue properties

The fatigue life of undamaged smooth-bar specimens was significantly affected by prior high-velocity impact damage, as clearly illustrated by the stress-life (S–N) data in Fig. 6. Previously published fatigue data [16], tested at a frequency of 85 Hz, are shown together with additionally tested 1000 Hz data. At a far-field maximum stress of 500 MPa ($R = 0.1$), which represents the 10^7-cycle fatigue limit [1] for undamaged

[1] 10^7 cycles fatigue limit of $\sigma_{max} = 500$ MPa was derived from the data shown in Fig. 6. These data have been more recently confirmed by the results of Bellows et al. [17] at the 10^7 cycle limit, and by ourselves at the 10^8 cycle limit; all these data suggest a fatigue limit of 500 MPa.

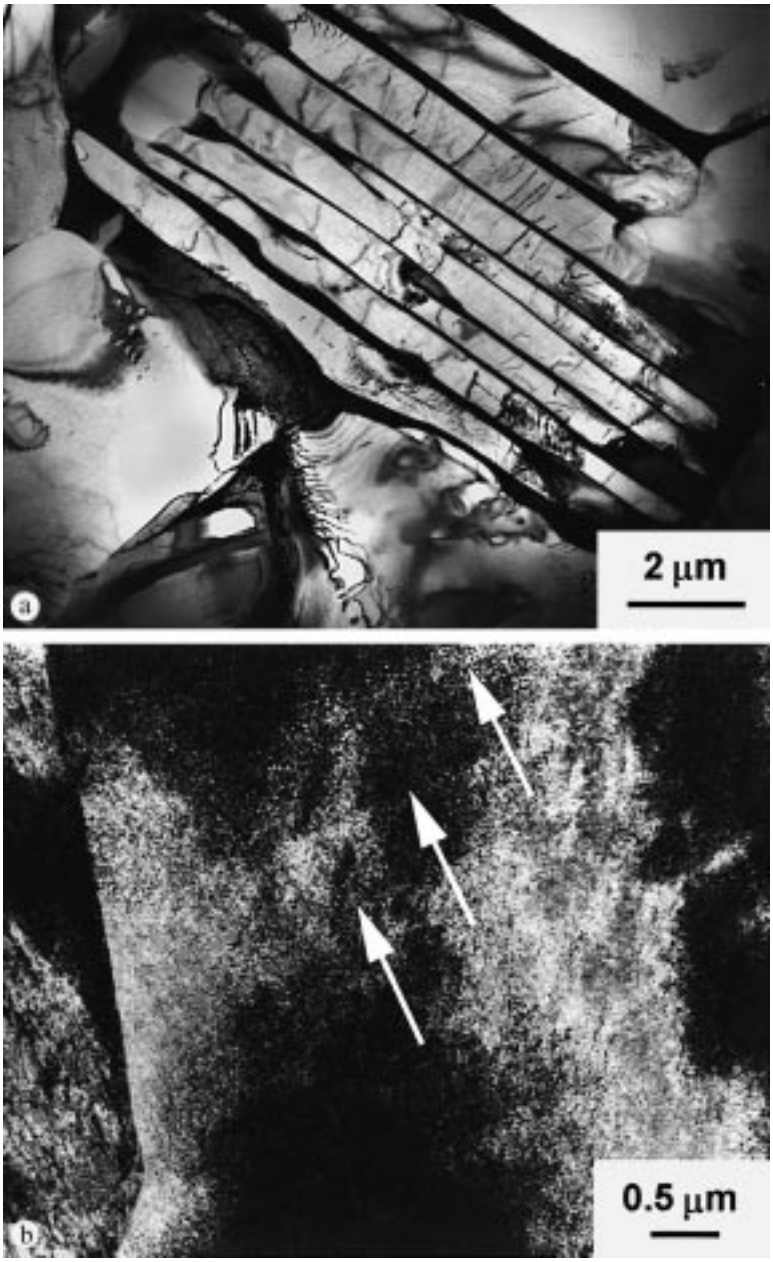

Fig. 5. Transmission electron microscopy bright-field images of (a) undamaged microstructure showing globular primary α phase within lamellar $\alpha + \beta$ matrix (alternating α lamellae (bright contrast) and β lamellae (dark contrast)) and (b) 300 m/s impacted microstructure located close to the base of the indentation site. After high-velocity impact, the microstructure shows very high density of very small dislocations with some dislocations, specifically within the primary α phase, arranged in preferred microbands (arrows).

material, final failure in the damaged material occurred between $\sim$4 and 10×10^4 cycles. These results show that FOD severely reduced fatigue lives, by over two orders of magnitude, compared to smooth-bar properties.

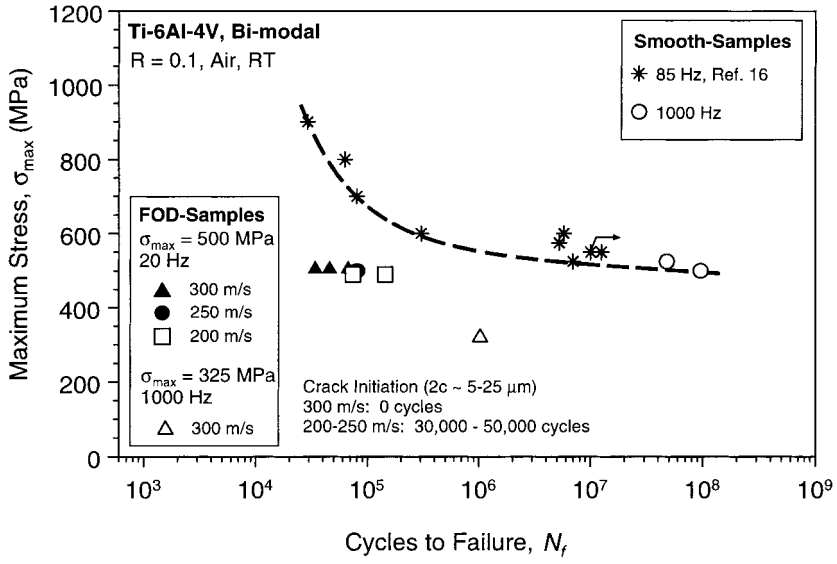

Fig. 6. S–N data show reduced fatigue life due to simulated FOD as compared to smooth-bar specimens in bimodal Ti–6Al–4V. Previously published results shown from Ref. [16] are complemented by 1000 Hz data.

3.2.1. FOD-induced crack initiation

With respect to the crack initiation at FOD impact sites (Fig. 7), the location of the initiation sites was found to depend strongly on impact velocity. For 300 m/s impact, fatigue cracks initiated from FOD-induced microcracks at the crater rim (Fig. 7a), whereas for lower velocity impacts (200–250 m/s), surface cracks tended to form at the base of the indentation site, as shown in Fig. 7b.

The change in crack nucleation mechanisms with impact velocity results from the interplay of stress concentration, the presence of microcracking and residual stresses. The crater rim and the base of the FOD indents are regions of high stress concentration [9]. Furthermore, the crater rim is a region of tensile residual stresses, whereas the base of the indent is a region of relatively low compressive residual stresses [14]. The stress concentration at the base of the indent, though, is always larger than that at the crater rim (Table 3); this coupled with the absence of microcracking at the lower impact velocities (200–250 m/s) and low compressive residual stresses leads to premature crack initiation at the indent base. Indeed, for such lower velocity impacts, the damage sites are relatively shallow such that the effective-fatigue stress-concentration factors (measured from the S–N data in Fig. 6) are essentially identical to the computed theoretical elastic values, i.e., $k_f \sim 1.4$, $k_t \sim 1.4$–1.5 (Table 3).

For the high velocity impact (300 m/s), conversely, FOD-induced microcracking in the pile-up region of the impact crater rim provides the dominant site for the initiation of fatigue cracks on subsequent cycling. In addition, tensile residual hoop stresses (estimated in Ref. [14]), the highly deformed microstructure in this region (Fig. 5b), and the slightly lower stress-concentration factors ($k_t \sim 1.25$, compared to $k_t \sim 1.6$ at the indent base) are all contributing factors.

A further mode of crack initiation could be detected at the surface of the simulated FOD impact sites. Fig. 7c shows that even smallest dust particles from the test set-up (10 μm Si-containing particles) pressed into the surface by FOD impact resulted in a preferential crack nucleation site.

3.2.2. Fatigue thresholds and crack propagation

Thresholds for fatigue-crack growth and the subsequent near-threshold fatigue-crack growth rates were measured on all FOD-damaged samples; results are compared in Fig. 8 with previous results on this alloy

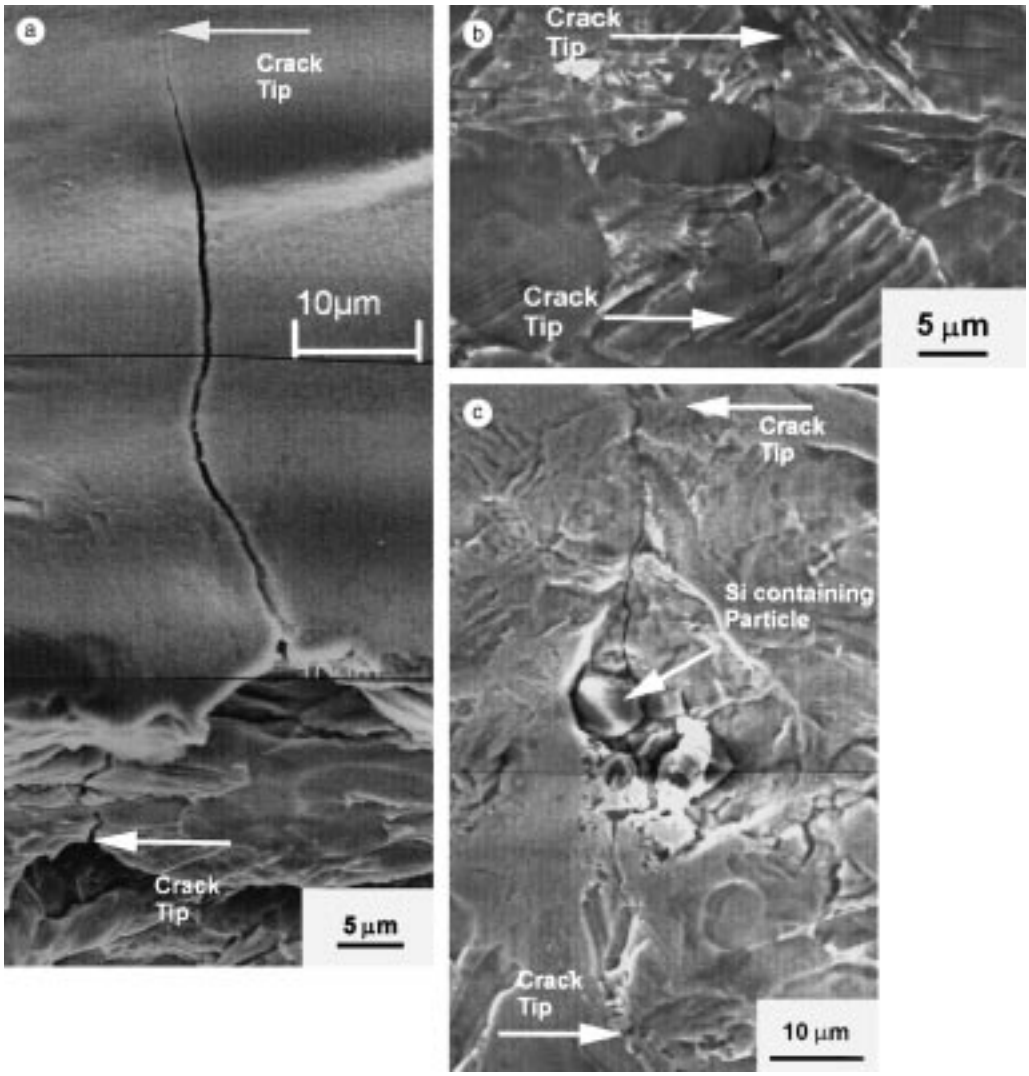

Fig. 7. Scanning electron micrographs of fatigue cracks that formed (a) at the pile-up of a 300 m/s impact velocity indentation crater (nominally applied $\sigma_{max} = 500$ MPa, $R = 0.1$, $N = 29{,}000$ cycles), (b) at the base of a 200 m/s impact velocity indentation crater (nominally applied $\sigma_{max} = 500$ MPa, $R = 0.1$, $N = 54{,}000$ cycles), and (c) at a Si containing dust particle that was pressed into the base of a 300 m/s impact velocity indentation crater (nominally applied $\sigma_{max} = 500$ MPa, $R = 0.1$, $N = 24{,}000$ cycles).

for the behavior of naturally initiated small (~45–1000 μm) cracks [16] and through thickness large (>5 mm) cracks [18] in undamaged material. The small crack growth-rate data are shown as a function of surface crack length, $2c$, and of the applied stress-intensity range (corrected for the stress concentration of the indent using Eq. (2)). For the FOD-induced small cracks, growth rates at $R = 0.1$ can be described by following best-fit relationship (units: m/cycle, MPa $\sqrt{}$m):

$$da/dN = 10^{-10}(\Delta K)^{2.8}. \quad (2)$$

It can be seen that FOD-initiated small-crack growth rates are aligned within a scatter band that approximately varies between the large-crack data (as a lower bound) and naturally initiated crack data (as an

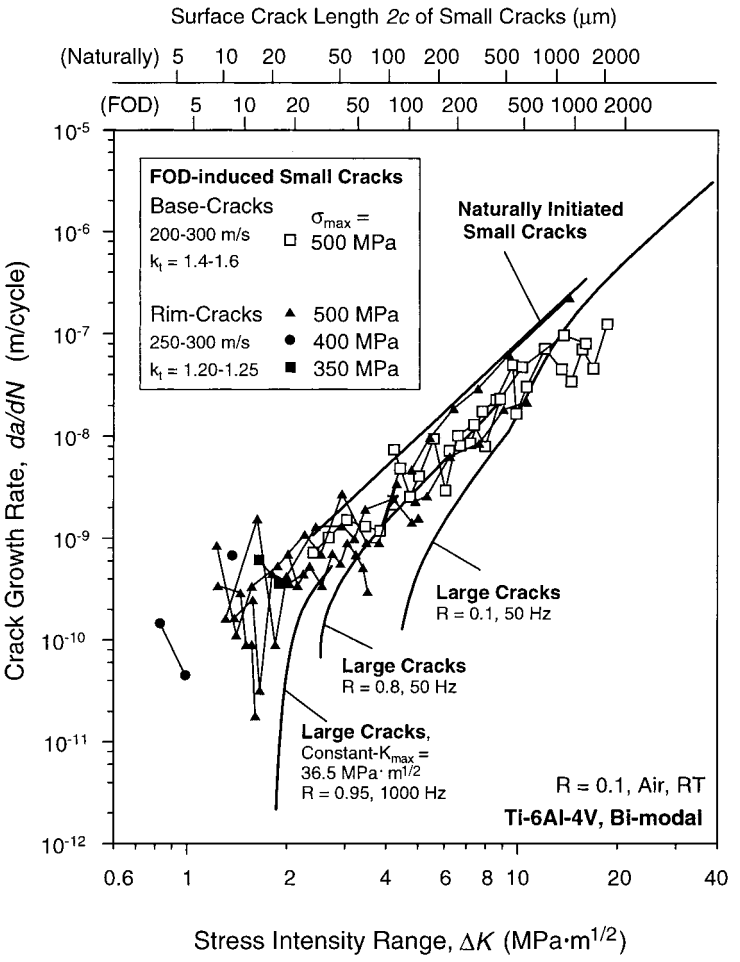

Fig. 8. Comparison of crack-growth rates, da/dN, as a function of applied stress-intensity range, ΔK, of FOD- and naturally-initiated small cracks and through-thickness large cracks in bimodal Ti–6Al–4V. Small cracks were initiated at $\sigma_{max} = 650$ MPa ($R = -1$) and the stress-intensity range was based only on the tensile portion of the loading cycle [16]. Large-crack growth data for $R \leqslant 0.8$ were derived from constant load-ratio tests, whereas for $R \geqslant 0.8$, constant-K_{max}/increasing-K_{min} testing was used [5]. Stress-intensity data for FOD-initiated crack growth has been corrected for the stress concentration associated with the indent using the K solution of Lukáš [12] and stress-concentration factors from Ref. [13].

upper bound). There is also a tendency for the growth rates of the FOD-initiated cracks formed at the crater rim (rim cracks) to be slightly faster than those that formed at the base (base cracks). In general, the growth rates of the naturally and FOD-initiated small cracks are roughly an order of magnitude faster than corresponding large-crack results at near-threshold levels, i.e., typical for the small-crack effect (see e.g., Ref. [19]). Above a ΔK of $\sim$10 MPa $\sqrt{\text{m}}$, however, the large and small crack results tend to merge, consistent with the increased dimensions of the small cracks.

As discussed in detail elsewhere [5,18], the large-crack results in Fig. 8 were determined up to the highest load ratios ($R \sim 0.1$–0.95) under conditions (constant-K_{max}/increasing-K_{min}) chosen to minimize the effect of crack closure; the threshold of $\sim$1.9 MPa $\sqrt{\text{m}}$ at $R = 0.95$ is thus considered to be a "worst-case threshold" for cracks of dimensions large compared to the scale of the microstructure, i.e., for "continuum-sized" cracks. Of significance in the present results is that the smallest FOD-initiated cracks, which have

dimensions of ~2–25 μm, i.e., comparable with microstructural size scales, can propagate at stress intensities well below this "worst-case" threshold, specifically at applied stress intensities down to a $\Delta K \sim 1$ MPa $\sqrt{m}$. The implication of this result is that in the bimodal Ti–6Al–4V alloy, there is a definitive lower-bound ΔK_{TH} threshold (~1.9 MPa $\sqrt{m}$) for "continuum-sized"cracks, i.e., large or physically small cracks with dimensions larger than the characteristic microstructural size-scales; however, when crack sizes approach such microstructural size scales, crack growth at applied stress intensities considerably less than this threshold is possible, presumably due to biased sampling of the "weak links" in the microstructure by the microstructurally small crack.

With respect to the possibility of finding a similar well-defined threshold for cracks emanating from regions of impact damage, the present results indicate that FOD-initiated microcracks, with dimensions in the range ~2–25 μm, can readily propagate in Ti–6Al–4V at stress-intensity ranges as low as $\Delta K \sim 1$ MPa $\sqrt{m}$ at nominal maximum stresses from 325 to 500 MPa ($R = 0.1$); moreover, such small cracks show no pronounced threshold behavior. Indeed, it is believed that a ΔK of 1 MPa $\sqrt{m}$ is the lowest stress-intensity range ever measured for crack growth in Ti–6Al–4V, representing a ΔK value roughly a factor of two smaller than the lowest measured fatigue threshold for a "continuum-sized" crack.

It should be noted here that there are still some uncertainties in the calculation of the driving forces for the propagation of the FOD-induced "microstructurally" small cracks, specifically because of their size in relation to the scale of local cyclic plasticity (although maximum plastic-zone sizes are only on the order of ~0.2–1 μm for 1–10 μm sized cracks at $\Delta K \sim 1$–2 MPa $\sqrt{m}$), and because of the presence of both tensile and compressive residual stresses. Although residual stresses are not included in the calculation of K (Eq. (2)), as a first approximation such stresses do not change the stress-intensity range (ΔK); they affect the mean stress and hence alter the local load ratio. Residual stresses are being numerically analyzed using a quasi-static model [14]. Results for the lower velocity impacts (200 m/s) have been experimentally verified by X-ray micro-diffraction methods [15], but numerically results severely overestimate the measured residual stresses for 300 m/s impact, presumably due to rate-sensitive phenomena such as shear-band formation and local heating. The latter effect, the possible relaxation of residual stresses due to fatigue loading, and the appropriate method of superposition of the applied and residual stresses to estimate local driving forces, are currently under study.

It is clear that our previously stated argument [5,9,18] for the notion of a high-cycle fatigue threshold, which was based on the concept of a "worst-case" threshold (determined under $R \to 1$ conditions that minimize crack closure), applies strictly for "continuum-sized" cracks; it does not provide a lower-bound threshold stress intensity for cracks on the scale of microstructural dimensions, as in the earliest stages of FOD-induced fatigue failure. However, coupling the notion of the worst-case threshold stress intensity with the fatigue limit, as in the Kitagawa–Takahashi diagram [20], does provide an alternative approach to defining limiting conditions for HCF and FOD-related damage, as discussed below.

3.2.3. Threshold conditions based on the Kitagawa–Takahashi diagram

As an alternative HCF-design approach against FOD, which takes into account the presence of microstructurally small cracks, Fig. 9 shows the influence of crack size on the worst-case fatigue thresholds in the form of a modified Kitagawa–Takahashi diagram [20], where the stress range for a corresponding crack-growth threshold condition ($da/dN = 10^{-11} - 10^{-10}$ m/cycle) is plotted versus the crack length. According to the Kitagawa–Takahashi approach (solid lines), the stress range $\Delta\sigma$ for crack arrest is defined by the 10^7-cycle fatigue limit ($\Delta\sigma_{HCF} = 450$ MPa) with the fatigue-crack growth threshold (ΔK_{TH}) measured on "continuum-sized" cracks. El Haddad et al. [21] empirically quantified this approach by introducing a constant (intrinsic) crack length $2c_0$, such that the stress intensity is defined as $Y\Delta\sigma\sqrt{\pi(2c + 2c_0)}$, where Y is the geometry factor. The present results, plotted in this format in Fig. 9, show that crack growth from FOD-induced microstructurally small cracks can apparently occur at *nominal* stress ranges (closed symbols) below the Kitagawa/El Haddad limit, defined by the worst-case ΔK_{TH} threshold and 10^7-cycle fatigue limit;

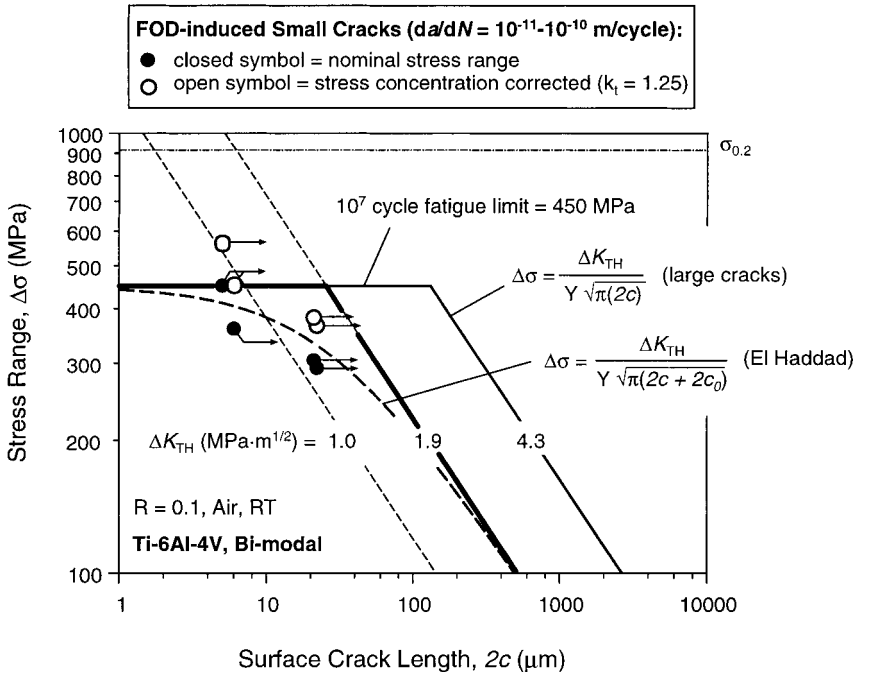

Fig. 9. Crack growth conditions of FOD-induced "microstructurally" small cracks ($da/dN = 10^{-11} - 10^{-10}$ m/cycle) as a function of cyclic stress range and surface crack length are shown in a modified Kitagawa–Takahashi diagram. Crack growth conditions were calculated for nominal (closed symbols) and stress-concentration corrected stress ranges (open symbols), and compared to smooth-bar 10^7-cycles fatigue limit and "continuum" large-crack growth threshold (solid line) and to a small-crack growth threshold model based on the solution given by El Haddad et al. [21] (dashed curve).

however, if these stresses are corrected for the effect of the stress concentration associated with the FOD indent (open symbols), crack growth occurs above the Kitagawa/El Haddad limit.

4. Summary and conclusions

Based on a study of the role of FOD on thresholds for high-cycle fatigue in a turbine blade Ti–6Al–4V alloy, involving considerations of (i) the stress concentration associated with the FOD indentation, (ii) FOD-induced microcracks, (iii) the localized presence of residual stresses, and (iv) microstructural damage from FOD-induced plasticity, the following conclusions can be made:

(1) Simulated high-velocity (200–300 m/s) FOD impact of steel spheres on a flat surface was found to markedly degrade resistance to high-cycle fatigue. For example, 200–300 m/s impacts on smooth-bar samples reduced the fatigue life by some two orders of magnitude at an applied stress corresponding to the smooth-bar 10^7-cycles fatigue limit ($R = 0.1$), an effect that is related to earlier crack initiation.

(2) The principal effect of FOD in reducing fatigue life was found to induce preferred sites for the premature initiation of fatigue cracks. For lower impact velocities (200–250 m/s), such initiation occurred at the base of the impact sites, where the stress concentration was highest. Conversely, at higher impact velocities (250–300 m/s), initiation occurred at FOD-induced microcracks in the pile-up of material around the impact crater rim.

(3) At nominal maximum stresses from 325 to 500 MPa ($R = 0.1$), FOD-initiated microcracks (~2–25 μm in size) propagated at applied stress intensities as low as $\Delta K = 1$ MPa $\sqrt{m}$ and showed no pronounced threshold behavior. This is well below the "worst-case" ΔK_{TH} threshold of 1.9 MPa $\sqrt{m}$ for "continuum-sized" cracks (i.e., cracks larger than the characteristic microstructural size scales) in this alloy. Such FOD-induced fatigue cracks propagated at rates roughly an order of magnitude faster than corresponding large (>5 mm) cracks at the same applied stress-intensity range. Small cracks initiated at the rim of the indentation sites appeared to grow at rates slightly faster than the cracks that initiated at the base.

(4) Correspondingly, the critical condition for HCF in the bimodal Ti–6Al–4V in the presence of "continuum-sized" cracks (of a size >50–100 μm) can be defined in terms of the "worst-case" fatigue threshold (determined under $R \rightarrow 1$ conditions that minimize crack closure). However, this concept alone is inappropriate where microstructurally small cracks (of a size ~2–50 μm) are relevant.

(5) For FOD-initiated failures, where the critical condition for HCF must be defined in the presence of microstructurally small cracks, the Kitagawa–Takahashi diagram is more appropriate, where the limiting conditions are defined in terms of the stress-concentrated corrected 10^7-cycle fatigue limit (at microstructurally small cracks sizes) and the "worst-case" ΔK_{TH} fatigue threshold (at larger, "continuum-sized" crack sizes).

Acknowledgements

This work was supported by the Air Force Office of Science and Research, grant no. F49620-96-1-0478, under the Multidisciplinary University Research Initiative on "High Cycle Fatigue" to the University of California, Berkeley. Special thanks are due to Prof. Werner Goldsmith (UCB) for providing the compressed-gas gun facility.

References

[1] Cowles BA. High cycle fatigue in aircraft gas turbines – an industry perspective. Int J Fract 1996;80:147–63.
[2] Nicholas T, Zuiker JR. On the use of the Goodman diagram for high cycle fatigue design. Int J Fract 1996;80:219–35.
[3] Larsen JR, Worth BD, Annis Jr CG, Haake FK. An assessment of the role of near-threshold crack growth in high cycle fatigue life prediction of aerospace titanium alloys under turbine engine spectra. Int J Fract 1996;80:237–55.
[4] Ritchie RO. Small cracks and high-cycle fatigue. In: Chang JCI, Coulter J, Brei D, Martinez WHG, Friedmann PP, editors. Proc ASME Aerospace Div, AD-vol. 52, ASME, Warrendale, PA, 1996. p. 321–333.
[5] Ritchie RO, Davidson DL, Boyce BL, Campbell JP, Roder O. High-cycle fatigue of Ti–6Al–4V. Fatigue Fract Engng Mat Struct 1999;22:621–31.
[6] Erosion, Corrosion and Foreign Object Damage Effects in Gas Turbines, AGARD Conference Proceedings No. 558, North Atlantic Treaty Organization. Advisory Group for Aerospace Research and Development, Propulsion and Energetics Panel, Neuilly-sur-Seine, France, 1994.
[7] Nicholas T, Barber JR, Bertke RS. Impact damage on titanium leading edges from small hard objects. Expt Mech 1980;20:357–64.
[8] Hudak SJ, Chan KS, McClung RC, Chell GG, Lee Y-D, Davidson DL. High cycle fatigue of turbine blade materials, Final Technical Report UDRI Subcontract No. RI 40098X SwRI Project No. 18-8653, 1999.
[9] Peters JO, Roder O, Boyce BL, Thompson AW, Ritchie RO. Role of foreign object damage on thresholds for high-cycle fatigue in Ti–6Al–4V. Metall Mater Trans A, 2000;31A, in press.
[10] Eylon D. Summary of the available information on the processing of the Ti–6Al–4V HCF/LCF program plates. University of Dayton Report, Dayton, OH, 1998.
[11] Sheldon JW, Bain KR, Donald JK. Investigation of the effects of shed-rate, initial K_{max}, and geometric constraint on K_{th} in Ti–6Al–4V at room temperature. Int J Fatigue 1999;21:733–41.
[12] Lukáš P. Stress intensity factor for small notch-emanating cracks. Engng Fract Mech 1987;26:471–73.
[13] Nisida M, Kim P. Stress concentration caused by the presence of a spherical cavity or a spherical-surfaced hollow. In: Proceedings of the Twelth National Cong Appl Mech, 1962. p. 69–74.

[14] Chen X, Hutchinson JW. Foreign object damage and fatigue cracking: on the shallow indentation. Int J Fract, Harvard University Report No. ME 358, Nov. 1999, in press.
[15] Boyce BL, Thompson AW, Roder O, Ritchie RO. Measurement of residual stresses in impact-damaged Ti–6Al–4V. In: Henderson J, editor. Proccedings of the Fourth National Turbine Engine High Cycle Fatigue (HCF) Conference, University Technology Corp. Dayton, OH, 1999, CD-Rom, Session 10. p. 28–40.
[16] Hines JA, Peters JO, Lütjering G. Microcrack propagation in Ti–6Al–4V alloys. In Boyer RR, Eylon D, Lütjering G, editors. Fatigue behavior of titanium alloys. Warrendale, PA: TMS,1999. p. 15–22.
[17] Bellows RS, Muju S, Nicholas T. Validation of the step test method for generating Haigh diagrams for Ti–6Al–4V. Int J Fatigue 1999;21:687–97.
[18] Ritchie RO, Boyce BL, Campbell JP, Roder O, Thompson AW, Milligan WW. Thresholds for high-cycle fatigue in a turbine engine Ti–6Al–4V alloy. Int J Fatigue 1999;21:653–62.
[19] Ritchie RO, Lankford J. Small fatigue cracks: a statement of the problem and potential solutions. Mater Sci Engng 1986;84:11–6.
[20] Kitagawa H, Takahashi S. Applicability of fracture mechanics to very small cracks or the cracks in the early stage. In Proceedings of the Second International Conference on Mechanical Behavior of Materials, ASM, Metals Park, OH, 1976. p. 627–31.
[21] Haddad MH, Topper TH, Smith KN. Prediction of non propagating cracks. Engng Fract Mech 1979;11:573–84.